Investigation on stability of large bedding slope affected by weak interlayer creep deformation

Fei Zhang[1,2] · Tianhong Yang[3] · Shaohua Li[4]

Abstract

The creep behavior of a weak interlayer inside the bedding slope is a main factor leading to the instability of a slope. Due to the creep of the weak interlayer, a large deformation has appeared in the large bedding slope in Fushun West Open-pit mine. In this study, to unveil the mechanism of the influence of strength reduction on the stability of the slope, experimental, theoretical, and numerical studies are carried out on carbon mudstone from the weak interlayer in Fushun West Open-pit mine. The time–strain curve, shear creep rate, threshold of the accelerated creep, and crack evolution of the carbon mudstone are analyzed. The results show that the shear stress has an exponential relationship with the steady stage creep rate. There is a threshold of the strain for the accelerated creep stage of the carbon mudstone. The macrocracks accumulate in the specimen with a shear band rather than a shear surface. According to the experimental results, an elastic-viscoplastic creep model is established. Furthermore, the stability evolution law of the bedding slope is analyzed using numerical simulation, which is helpful to access the stability evolution features of the slope and formulate corresponding reinforcement measures in advance.

Article Highlights

1. The shear creep behaviors of the weak interlayer are investigated through the shear creep experiments.
2. A new shear creep model is proposed, and the dynamic parameters of the weak interlayer are obtained.

✉ S. Li
  lishaochina@163.com

1   Key Laboratory of Roads and Railway Engineering Safety Control, Ministry of Education, Shijiazhuang Tiedao University, Shijiazhuang 050043, China

2   School of Civil Engineering, Shijiazhuang Tiedao University, Shijiazhuang 050043, China

3   School of Resources and Civil Engineering, Northeastern University, Shenyang Liaoning 110819, China

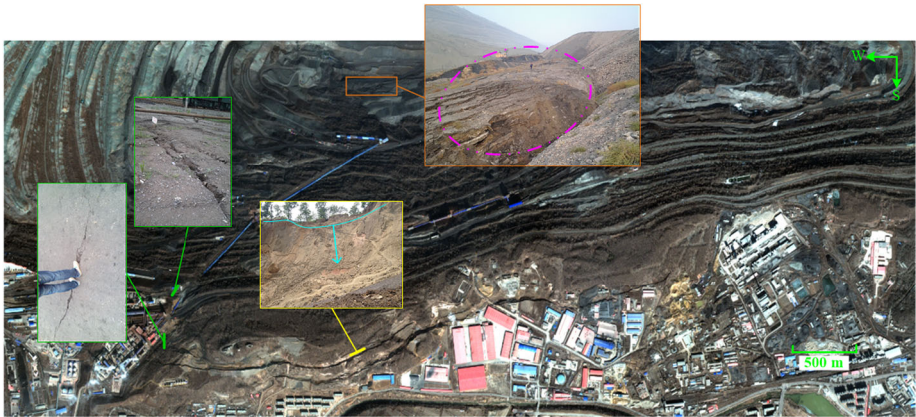4   School of Civil Engineering, Wuhan University, 430072 Wuhan, China

Fig. 1 The cracks observed on the surface of the south slope of Fushun West Open-pit mine

3. The influence of the creep deformation of the weak layer on the deformation evolution features of the slope is clarified by a numerical simulation method.

1 Introduction

The landslide disasters of the bedding slope are mostly related to the inner weak layers undergoing shear creep under the weight of the upper rock mass. A number of studies have shown that the instability of the slope is attributed to the large creep deformation rather than the low strength of the soft rock mass (Liu et al. 2020b; Zhao et al. 2020a; Xu et al. 2014). Thus, the influence of the creep behaviors of the weak layer on the stability of the slope is nonnegligible. The south slope of Fushun West Open-pit mine is a typical deep and large bedding slope, the maximum height of which is 400 m. There is a carbon mudstone weak layer inside the slope. Due to the long-term creep deformation of the weak layer along with the excavation, some macrocracks, bottom heave, and large deformation appeared since 2009 (Fig. 1). The large long-term creep deformation of the slope has threatened the safety of operation and citizens around the mine. Therefore, understanding the creep behaviors of the weak layers, especially for the deep and large bedding slope, is helpful in the stability assessment and reinforcement of the slope.

Field monitoring is the direct method to obtain slope deformation information. Slope monitoring technology is mainly divided into surface monitoring (Manconi et al. 2018; Rahardjo et al. 2018) and underground monitoring (Xu et al. 2011). Although the on-site monitoring has many advantages for studying the deformation characteristics of slopes, it is difficult to reveal the internal deformation mechanism of slopes due to the limitation of monitoring cost and scope. Therefore, many scholars began to study the deformation mechanism of slopes by means of laboratory experiment and numerical simulation. To acquire the creep behaviors of geotechnical materials, many scholars have conducted research using different methods, including indoor experiment, numerical methods, etc. Therefore, many scholars have carried out researches on rock (Wang et al. 2020; Zhao et al. 2017; Liu and Zhao 2021), structural planes (He et al. 2019; Wu et al. 2016), and soil (Hou et al. 2018; Li et al. 2019; Chang et al. 2020) by means of indoor experiment. Indoor tests are also often used to study the creep characteristics of the sliding zones. For example, Lai et al. (2010)

conducted a series of creep experiments of sliding zones and proposed a creep model. Deng et al. (2016) carried out a series of creep experiments to study the creep behaviors of the soft rock and the effect on the stability of the bank slope. Besides, some scholars have carried out research on the creep characteristics by numerical simulation (Li et al. 2017; Wang et al. 2017; Zhou et al. 2020; Fu et al. 2020; Mikroutsikos et al. 2021). The numerical methods can reproduce the creep deformation process and predict the deformation trend. However, the accuracy of the calculation is always based on the credible experimental results and the creep model.

Based on the study of creep behavior, creep theory has also been fully developed. At present, there are mainly four types of models for the description of creep characteristics, which are empirical model (Wei et al. 2021; Liu et al. 2020a), element model (Lin et al. 2020; Huang et al. 2020), viscoelastic-plastic model (Wu et al. 2020; Huang et al. 2021), and fracture damage model (Liu et al. 2021; Yuan et al. 2021). The element model was widely used and popular in the study of creep models. Some scholars proposed new models to describe the creep behaviors of geotechnical materials, such as rocks and sliding zone soils (Hou et al. 2019; Sun et al. 2016; Chang et al. 2020). In order to describe the accelerating creep stage, more complex models have been proposed by considering more viscous and elastic elements. However, the numerous parameters do not have a clear physical meaning (Xu et al. 2013). Therefore, the element model is always used combining with viscoplastic and damage element (Wu et al. 2019; Lin et al. 2020). Some scholars embed the proposed creep model into the numerical software and reproduce the creep process, achieving good results (Chen et al. 2017; Yu et al. 2018). However, due to the limitation of time and professionalism on-site, this method is not friendly enough to field applications. Thus a convenient method should be put forward.

This study aims to unveil the stability evolution of the bedding slope with a weak interlayer, combining experimental, theoretical, and numerical methods. Firstly, the relationship between the steady stage creep rate and the shear stress is studied. In addition, the creep features at failure shear stress level are analyzed, and the ultimate strain is obtained. Then, the failure characteristics and the shear strain features of the carbon mudstone are studied. Based on the experimental results, a modified nonlinear six-component rheological model is established, and the time-varying dynamic shear strength parameters are acquired. Finally, the stability of the south slope of Fushun West Open-pit mine, considering the decay of shear strength of the weak interlayer caused by creep behaviors, is investigated. The results in this study shed light on the stability evolution of the bedding slope.

2 Engineering background

The south slope of Fushun West Open-pit mine located in Liaoning province, Northeast China, was employed in this study. As one of the largest open-pit mines in the world, it is 6.6 km in the east–west direction and 2.2 km in the north–south direction. The main products of the open pit are coal and oil shale. The south slope of the open-pit mine belongs to a deep and large bedding slope. The maximum height of the slope is 400 m. The geological conditions of the south slope are quite complex due to the existence of natural faults, weak interlayers, and strong weathering. The overall tectonic stability is poor. The geological strata of the south slope of the Fushun West Open-pit mine are mainly composed of Quaternary topsoil, basalt, weak interlayer carbon mudstone which is located in the middle of the basalt, and granite gneiss from the top to the bottom. The main faults, including f5, f5-1, f5-2, f5-3, f2, f3, and f3-1, are distributed in the south slope. The fault f5 is located

in the middle of the south slope and changes the constraint condition of the slope. Qiantai Mountain is located at the top of the study area, and its north slope is connected to the south slope of the mine, with an elevation of +214 m. The study area is a hilly area with large fluctuation, and the mining area is a terrace formed by artificial transformation. The south slope is a non-working slope. Since the excavation of the south slope, the soil on the surface of the south slope has been stripped off and the basalt has been gradually exposed. Owing to excavation unloading, the stability problem of the slope has been further aggravated. Based on the drilling survey results, the weak layer is located in the middle of the basalt. Meanwhile, owing to the continuous deformation of the slope, weak interlayers in some areas at the top of the south slope have been exposed. The weak layer is mainly located in the south slope, extending from the west to the east.

The slope stability problem is a concern for the mine and the government. For instance, the green mudstone with fold structure in the north slope is constantly deformed until a large deformation occurs. The power plant and the oil plant near the slope had to be relocated. This caused great losses to the local government. Due to the continuous excavation and long-term creep deformation of the weak interlayer, the persistent deformation has gradually appeared in the south slope since 2009. Some cracks in the slope have been discovered in the west and top of the slope and heave has also been observed at the bottom as shown in Fig. 1. The long-term creep of the weak interlayer significantly affected the overall stability of the slope (Li and Cheng 2021). A large landsliding block has gradually formed as a result of the deformation in the south slope. The south boundary of the sliding block located at the top of the slope is Qiantai mountain crack. The east boundary is the fault f5. The west boundary is near the W700 section extending from the top to the bottom. According to the deformation features and geological conditions, the backfill presser foot reinforcement measures were implemented in 2013 to ensure the overall stability of the south slope. The backfill projects were mainly concentrated at the bottom of the west region of the open-pit mine, only a few parts were implemented in the east region at the bottom of the open pit.

3 Experimental materials and methodology

3.1 Experimental materials

The carbon mudstone sample used in this test was taken from the south slope of Fushun West Open-pit mine, and the color of the large block is black. In order to reduce the influence of the discreteness of rock samples on the test results, all the samples used in this study were obtained from the same block, and the processed samples are shown in Fig. 2. In order to ensure the reliability of the experimental results, we selected three groups of samples for repeated experiment. Furthermore, the wave velocities of three directions of the sample were screened by an acoustic wave detection device, and the samples with a large difference in the wave velocity ($> \pm 100$ m/s) were eliminated while the samples with a similar acoustic wave velocity ($\leq \pm 100$ m/s) were used for the test. The acoustic wave velocity of carbon mudstone samples is listed in Table 1. The length, width, and height of the sample were 50 mm.

3.2 Experimental methodology

A rock creep test instrument was used in the experiment. It is composed of four parts: a loading system, a data acquisition system, a high-pressure oil pump station, and a test machine.

Fig. 2 Samples of carbon mudstone

Table 1 Acoustic wave velocity of carbon mudstone samples

Normal stress (MPa)	Shear stress (MPa)	X-direction velocity (km/s)	Y-direction velocity (km/s)	Z-direction velocity (km/s)
1	0.58	2.809	2.812	2.795
	1	2.846	2.771	2.786
	1.73	2.862	2.846	2.815
3	1.73	2.796	2.825	2.777
	3	2.801	2.843	2.810
	5.20	2.851	2.842	2.803
5	2.89	2.820	2.821	2.796
	5	2.854	2.798	2.806
	8.66	2.785	2.798	2.842
7	4.04	2.781	2.793	2.775
	7	2.815	2.799	2.821
	12.12	2.809	2.792	2.860

The shear creep test under different shear stress levels was carried out by changing the angle of the direct shear head. In this experiment, the shear stress of the specimen under same normal stress conditions was loaded step by step by changing the angle of the direct shear head. Three direct shear heads with different angles were used in this test, and the angles were 30°, 45°, and 60°, respectively. Figure 3 shows the direct shear head of 45°. Vaseline was used at the end of the specimens to reduce the friction between the samples and shear head.

The conventional creep experiment method was selected to investigate the influence of shear creep behaviors of carbon mudstone. The conventional creep experiment method is that the shear stress level is kept constant till the failure of specimens and the deformation and failure time under a stress level can be obtained (Lade et al. 2009). In order to calculate the overburden loading on the weak interlayer, the weak interlayer and the overlying layer are both simplified as a rectangular strip. Then, different sections are selected for calculation. According to the overburden loading on the weak interlayer of the south slope of Fushun West Open-pit mine, the corresponding normal loading force of the experiment was calculated, and then four representative normal stress loads were determined. Three shear creep loading levels were carried out under each level of normal stress, and then the load-
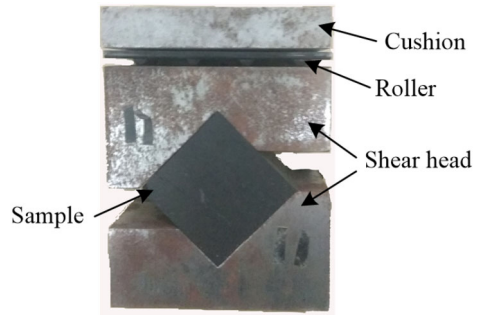
Fig. 3 The shear head of the creep test

Table 2 The applied stress of the shear creep experiment

Normal stress (MPa)	Shear stress (MPa)		
	60° shear head	45° shear head	30° shear head
1	0.58	1	1.73
3	1.73	3	5.20
5	2.89	5	8.66
7	4.04	7	12.12

ing scheme was determined as listed in Table 2. Under different levels of shear loading, the crack propagation and creep behaviors in the shear creep test were obtained, and the data were recorded.

The setting time of each shear stress level in this test is 10~15 h initially. When the deformation of the specimen is less than 0.001 mm within 1 h, the specimen was unloaded; then, another specimen was loaded to a higher shear loading level. The load sensor was used to record the loading of the test, the laser displacement system was used to record the deformation of the sample, and digital image correlation method (DIC) was used to monitor the strain on the surface of the sample.

DIC has been widely used to characterize the deformation of rock materials (Zhou et al. 2018; Yang et al. 2020). The basic principle of DIC is to match the geometric points on the digital speckle image in different states of the object surface, and track the movement of the points to obtain the surface deformation information of the object (Zhao et al. 2020b). The schematic diagram of the DIC testing system is shown in Fig. 4. The hardware system consisted of a high-speed camera, a camera trigger device, an image capture card, a monitor, a computer, and an A/D card. The software system was used to process the speckle images collected in the experiment, and then obtain the required deformation information, including strain and correlation coefficient distribution information. In the process of the creep test, the speckle testing system was also used to monitor the whole process of the creep behavior of carbon mudstone. The surface of the specimen was painted with speckles.

During the creep deformation process of the specimen, some specific marking points were selected to investigate the creep behaviors. Because the specimen was placed obliquely during the test, only the deformation characteristics of the rectangular area at the center of the specimen were studied when the test results were postprocessed (Fig. 5).

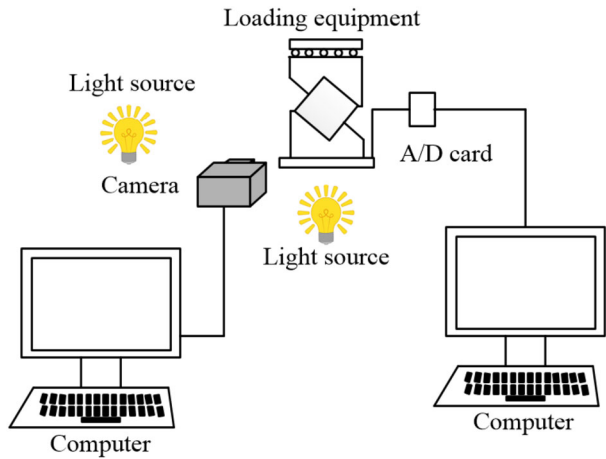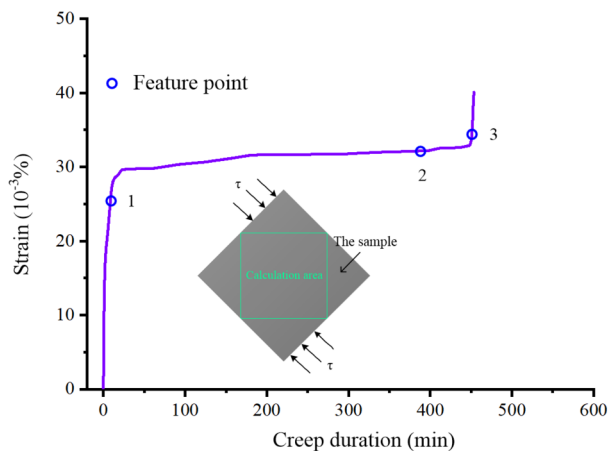**Fig. 4** The schematic diagram of speckle system

Fig. 5 The calculation area and the position of feature point of the sample

4 Experimental results

4.1 Time–strain curve

According to the experimental results (Fig. 6), it can be seen that the carbon mudstone exhibits three creep stages under the normal stress of 3, 5, and 7 MPa. Under normal stress of 1 MPa, it can be seen from the time–strain curve that the specimen only exhibits the primary creep and the steady creep stage, but no accelerated creep stage. This phenomenon can be attributed to that the shear stress level is not high enough to meet the condition of the accelerated creep stage. It is also shown that the initial strain was produced with the application of shear loading. At the same time, the shear strain also increased with the increasing of the shear loading. Due to the different level of the shear loading, the structure inside the specimen changed differently. During the creep process, the original microcracks were compacted and the new cracks experienced initiation, propagation, and interaction (Wang et al. 2013).

Under a lower shear stress level, the deformation of the specimen is basically stable at a value after a short period of primary creep stage. During this process, there are not many
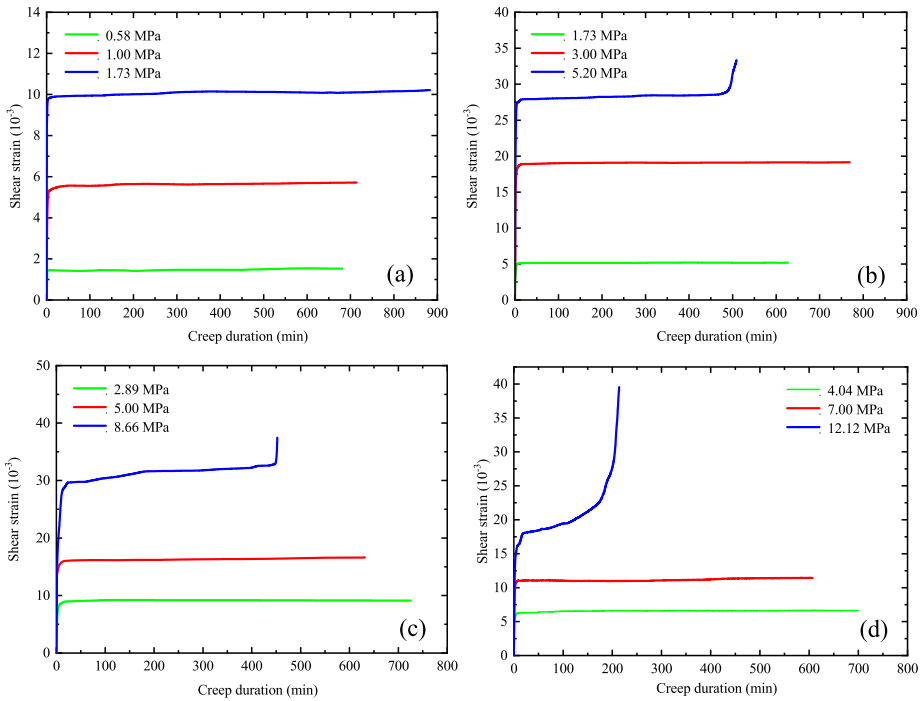
Fig. 6 The time–strain curve under different normal stress: (a) 1 MPa; (b) 3 MPa; (c) 5 MPa; and (d) 7 MPa

crack penetrations, and the deformation of the specimen gradually stabilizes while when the specimens are placed under a higher stress level, the microcracks are further generated and propagate, and the density of the microcracks also increases. The bearing capacity of the specimen decreases, and the deformation obviously increases. Furthermore, the macroscopic cracks gradually penetrated, and the specimens were destroyed. There are also three stages of shear creep rate corresponding to the three creep stages.
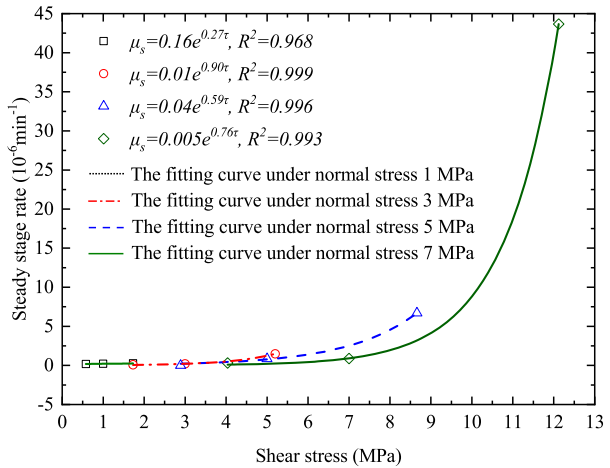
4.2 Steady state creep rate

Analyzing the creep rate at the steady creep stage of the rock is significant to determine the magnitude of the creep strain produced during the same time. The steady creep stage is the main component of rock shear creep. Figure 7 shows the relationship between the steady creep rate and the shear stress. It can be seen that under the same shear stress level, the small normal stress level will produce a large shear creep rate at the steady creep stage. The creep rate increases with the increase of the shear stress level under the same normal stress level. An exponential relationship between the steady creep rate and the shear stress is proposed as follows:

$$u_s = a e^{b\tau}, \tag{1}$$

where a and b are the parameters related to the rock mass; u_s is the steady creep rate, and τ is the shear stress.

**Fig. 7** Fitting curve of the steady stage creep rate

$\mu_s=0.16e^{0.27\tau}$, $R^2=0.968$
$\mu_s=0.01e^{0.90\tau}$, $R^2=0.999$
$\mu_s=0.04e^{0.59\tau}$, $R^2=0.996$
$\mu_s=0.005e^{0.76\tau}$, $R^2=0.993$

The fitting curve under normal stress 1 MPa
The fitting curve under normal stress 3 MPa
The fitting curve under normal stress 5 MPa
The fitting curve under normal stress 7 MPa

Steady stage rate (10^{-6} min^{-1})

Shear stress (MPa)

4.3 Creep characteristics at different shear stress levels

In order to study the characteristics of the carbon mudstone sample at the failure stage under different normal stress, the relationship between the shear strains, shear creep rate, and time are shown in Fig. 8. Due to the limitation of experimental conditions, the accelerated creep stage does not appear under the normal stress of 1 MPa. Therefore, the creep characteristics of specimens at the failure shear stress level under the normal stress of 3, 5, and 7 MPa are analyzed in this part. In case of the normal stress of 3 MPa, as shown in Fig. 8(a), the curve can be divided into three stages, OA, AB, and BC. The OA stage is the primary creep stage. The AB stage is the steady creep stage. The BC stage is the accelerated creep stage. In the OA stage, with the increase in loading time, the amount of strain continues to increase while the creep rate gradually decreases, and finally the creep rate gradually stabilizes. In the AB stage, the strain of the specimen increases slowly as time increases. At the same time, the creep rate is small and relatively stable. In the BC stage, both the creep strain and creep rate of the sample increase drastically until the sample is broken. In addition, it can be observed that when the normal stress is 5 MPa, the creep strain and creep rate have obvious jumps at the accelerated creep stage, which may be caused by the rapid penetration of the microcracks. It also can be seen that when the specimen enters the accelerated creep stage, the strain will increase sharply. It seems that there is a "strain threshold" of the accelerated creep stage.

4.4 The failure characteristics of the carbon mudstone

The failure type of the specimen under the normal stress of 3 MPa is shown in Fig. 9(a), which illustrates that the shear surface of the carbon mudstone sample is not a straight fracture surface. There are some rock fragments along fracture surfaces, and there are also obvious scratches near the shear surfaces. According to those phenomena, it can be speculated that the shear failure of the sample occurs on a shear zone with a certain thickness rather than a shear plane. From the phenomenon of specimen failure, the specimen is not strictly broken along the direction of the shear stress. During the shear fracture process, some tension cracks developed intersecting with the shear surface. These tension cracks started from the shear surface and gradually developed in the normal stress direction.
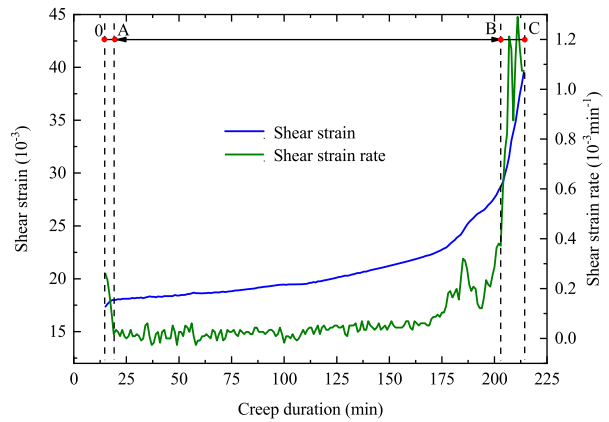
Fig. 8 Strain and strain rate characteristics of the carbon mudstone under different normal stress conditions: (a) 3 MPa; (b) 5 MPa; and (c) 7 MPa
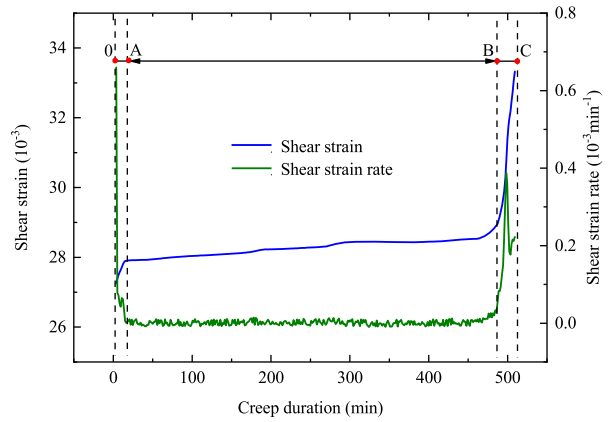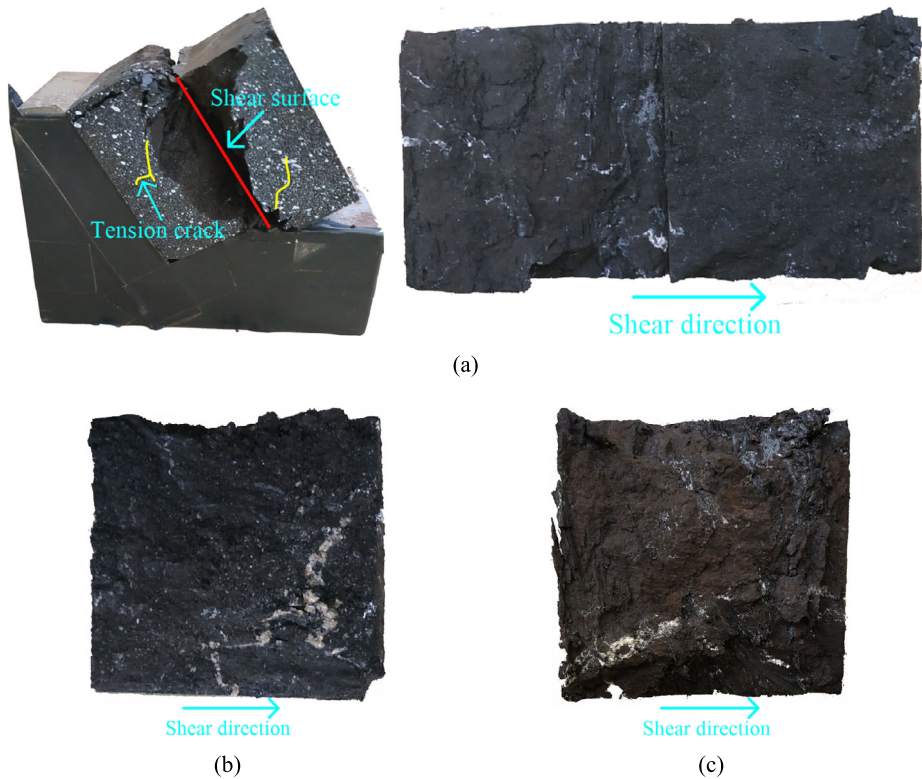

(a)
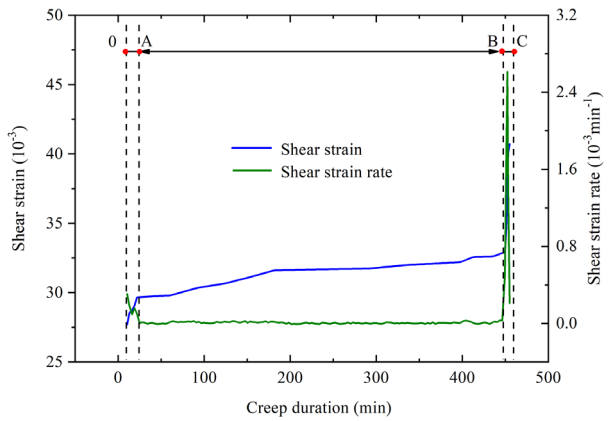
(b)

(c)

Fig. 9 Failure mode of a sample under different normal stress: (a) 3 MPa; (b) 5 MPa; and (c) 7 MPa

When the sample was placed under the same normal stress, while keeping the low shear stress level, the internal energy of the carbon mudstone accumulated continuously. With the application of the shear stress, the microcracks inside the sample gradually closed. However, the energy accumulation inside the sample did not reach the energy that can destroy the high-strength part supporting the integrity of the carbon mudstone. With the increase in shear stress level, stress concentration gradually appeared at both ends of the microcracks, and the energy inside the sample further increased. On the other hand, when shear stress level did not reach the failure stress level, the strain gradually increased, but there was no sharp increase of the strain. When the shear stress reached the failure level, the cracks in the high-strength part of the sample were continuously generated and propagated. When the cracks finally connected, a macroscopic shear fracture zone was formed inside the rock, and the sample was finally destroyed.

Then the samples were placed under a different normal stress and in the failure shear stress level. When the normal stress was 5 MPa, the shear zone gradually widened. At the same time, the rock fragments along the shear zone increased significantly. It is also shown that the scratches on the surface of the shear zone deepened (as shown in Fig. 9(b)). The number of tensile cracks intersecting the shear zone also increased. When the normal stress reached 7 MPa (as shown in Fig. 9(c)), the fracture area of shear zone was further increased. The amount of fragments on the surface of the shear zone increased and the particles were smaller than that for the normal stress of 3 and 5 MPa. Furthermore, the opening of the tensile cracks intersecting the shear zone dominantly increased. These features are similar
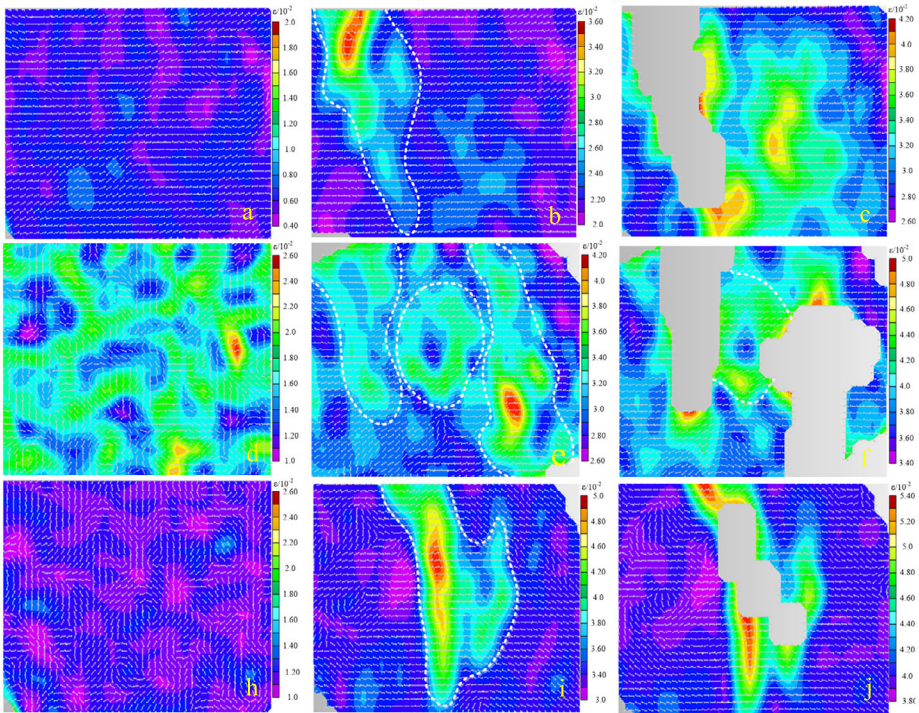
Fig. 10 The contours of the maximum shear strain under different normal stress: (a)–(c) feature points 1–3 under the normal stress of 3 MPa; (d)–(f) feature points 1–3 under the normal stress of 5 MPa; and (h)–(j) feature points 1–3 under the normal stress of 7 MPa

to the shear creep failure of the mudstone in the literature (Wu et al. 2017). The main reason for these phenomena is that, as the normal stress increases, the lateral restraining force of the sample gradually increases. The failure of the sample requires more accumulated energy. When the sample is damaged, it will cause serious damage due to the release of large amounts of energy.

4.5 Strain evolution characteristics

Figure 10 shows the evolution process of the maximum shear strain of the specimen at the failure shear stress level under different normal stress. Figure 10(a) presents the maximum shear strain contours at the primary creep stage. At this stage, the distribution of the shear strain is relatively uniform. When it reaches the late stage of the steady creep stage, the shear strain gradually concentrates towards the upper left corner (Fig. 10(b)). When the specimen enters the accelerated creep stage, the strain of the sample increases sharply, and macroscopic cracks gradually appear on the surface of the specimen, as shown in Fig. 10(c). In Fig. 10(c), due to the occurrence of macroscopic cracks on the surface of the specimen, the geometric points on the speckle image cannot be captured, resulting in strain field voids. Subsequently, with the continuous generation and propagation of cracks, the specimens were destroyed. Figure 10(d) shows a similar evolution law with the normal stress of 3 MPa. The difference is that in the primary creep stage there are different degrees of uneven distribution on the surface of the specimen, but there is no certain rule. This might be attributed to that

Fig. 11 Framework of creep model development
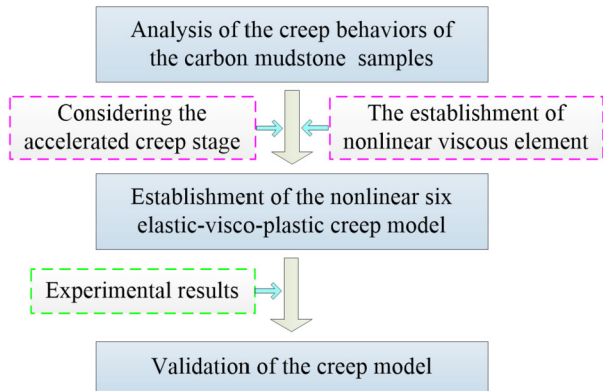
the pores in the specimen are adjusted to a certain extent at the primary creep stage, resulting in the uneven deformation of the sample surface. Thereafter, the surface crack expands along the upper and lower sides at the same time and finally penetrates in the middle of the sample, leading to the failure of the sample. Figure 10(i) and 10(j) illustrate that the macroscopic cracks on the surface are generated in the middle of the specimen, and eventually penetrate the specimen and cause damage to the specimen. Based on the DIC monitoring results, it can be found that the shear strain concentration phenomenon occurs in the corresponding position before the surface macrocracks appear. With an increase of the shear strain, the macrocracks are gradually generated along the shear strain concentration areas. Finally, the specimen undergoes shear failure along the macrocracks.

5 The establishment and validation of creep model

5.1 The establishment of creep model

The flow chart of creep development is shown in Fig. 11. To describe the shear creep features of the carbon mudstone, a creep model is considered. The behavior of the carbon mudstone samples is first analyzed and the Burgers model is selected to describe the primary and steady creep stage. Then, considering that the Burgers model cannot describe the accelerated creep stage of the carbon mudstone, the nonlinear viscous element is established and introduced into the creep model. Thereafter, the established model can be validated through the experimental results.

The creep deformation of rock generally goes through three stages under the high shear stress level. During the accelerated creep stage, the creep strain and creep strain rate will increase rapidly with time. The main reason is that the creep deformation of the rock is nonlinear at this stage, when the viscosity coefficient will gradually decrease with time. And when the crack is closed, it can be approximated that the viscosity coefficient is constant. Generally, the traditional component models can only describe the primary and steady creep stages of the rock mass. They cannot describe the process of mechanical deterioration of the rock mass and the process of accelerated creep stage. Thus, this study establishes a nonlinear plastic element based on the research of Gao et al. (2016) as shown in Fig. 12. For the new viscous element, the viscosity coefficient has a negative exponential function relationship with time as shown in Fig. 13.
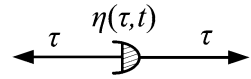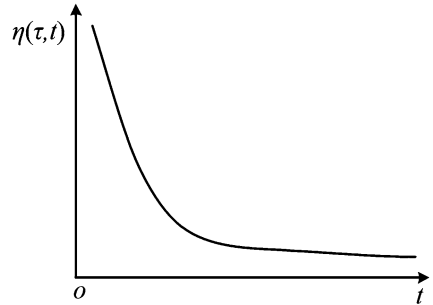
Fig. 12 Nonlinear viscous element

Fig. 13 Viscosity coefficient as a function of time

According to the Newton's law, the constitutive relationship of the viscous element can be expressed as

$$\tau = \eta(\tau, t)\dot{\gamma}, \tag{2}$$

where τ is the level of shear stress; η_P is the initial viscosity coefficient; and $\dot{\gamma}$ is the shear strain rate during shear creep deformation.

The expression of viscosity coefficient is as follows:

$$\eta(\tau, t) = \eta_P \, e^{\left[-\frac{H\langle\tau-\tau_s\rangle t}{a} - bH\langle\tau-\tau_s\rangle\right]}, \tag{3}$$

where $H\langle\tau - \tau_s\rangle = \begin{cases} 0 & \tau < \tau_s \\ \tau - \tau_s & \tau > \tau_s \end{cases}$; τ_s is the yield or long-term shear strength of the rock; a and b are the parameters related to the rock mass; and t is the rheological time of the rock mass.

According to the above relationship, the following relationship can be obtained:

$$\eta(\tau, t) = \eta_P, \quad \tau < \tau_s, \tag{4}$$

$$\eta(\tau, t) = \eta_P \, e^{\left[-\frac{(\tau-\tau_s)t}{a} - b(\tau-\tau_s)\right]}, \quad \tau > \tau_s. \tag{5}$$

When $\tau > \tau_s$, the constitutive relationship of the nonlinear viscous element can be obtained through Eqs. (2) and (5) as follows:

$$\gamma = \frac{a}{\eta_P}(e^{\left[\frac{(\tau-\tau_s)t}{a} + b(\tau-\tau_s)\right]} - e^{b(\tau-\tau_s)}). \tag{6}$$

Generally, the traditional element model can only describe the first two stages of creep. The accelerated creep stage cannot be described. According to the shear creep behaviors of carbon mudstone, at the initial creep stage, the carbon mudstone undergoes instantaneous deformation. Therefore, the spring element can be used to express this property. Then it can be found that it has a decelerating creep stage, so the Kelvin model can be used to describe this behavior. Thereafter, the carbon mudstone has an obvious accelerated creep stage, so a nonlinear viscous element can be used to describe this feature. In addition, the

Fig. 14 The nonlinear
six-element elastic-viscoplastic
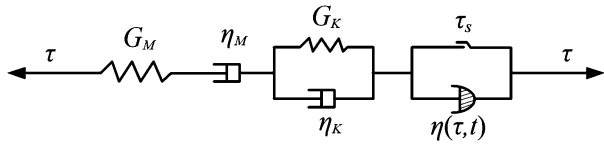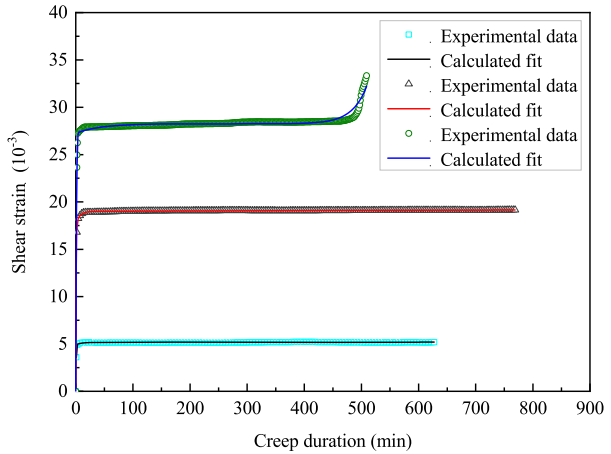rheological model

Fig. 15 The fitting result of the
creep test under the 3-MPa
normal stress

Burgers model and the above-mentioned nonlinear element model constitute a nonlinear six-element model to describe the whole creep stage of the carbon mudstone. The nonlinear elastic-viscoplastic model is shown in Fig. 14.

According to the relationship of the model, the total strain of the nonlinear elastic-viscoplastic model can be described as follows:

$$\gamma = \gamma_M + \gamma_K + \gamma_P, \tag{7}$$

where γ is the total strain of the improved nonlinear elastic-viscoplastic model, γ_M is the strain of the Maxwell model, γ_K is the strain of the Kelvin model, and γ_P is the strain of the nonlinear viscoplastic element model.

Therefore, the proposed nonlinear elastic-viscoplastic model can be expressed as follows:

$$\begin{cases} \gamma = \dfrac{\tau}{G_M} + \left(\dfrac{\tau}{\eta_M}\right)t + \dfrac{\tau}{G_K}\left(1 - e^{-\frac{G_K}{\eta_K}t}\right) & (\tau < \tau_s) \\ \gamma = \dfrac{\tau}{G_M} + \left(\dfrac{\tau}{\eta_M}\right)t + \dfrac{\tau}{G_K}\left(1 - e^{-\frac{G_K}{\eta_K}t}\right) + \dfrac{a}{\eta_P}\left[e^{\frac{\tau-\tau_s}{a}t+b(\tau-\tau_s)} - e^{b(\tau-\tau_s)}\right] & (\tau > \tau_s) \end{cases} \tag{8}$$

where G_M and η_M respectively are the shear modulus and viscosity coefficient of the Maxwell model while G_K and η_K respectively are the shear modulus and viscosity coefficient of the Kelvin model.

5.2 The validation of the elastic-viscoplastic model

In order to validate the proposed nonlinear elastic-viscoplastic model, the experimental results were used to analyze the reliability of the model. By comparing the experimental results with the proposed model calculated results, the fitting results in Fig. 15 show consistency,

Table 3 Model parameter inversion results under different shear stress level

Normal stress (MPa)	Shear stress (MPa)	Model parameters							R^2
		G_M (MPa)	η_M (MPa min)	G_K (MPa)	η_K (MPa min)	η_P (MPa min)	a	b	
3	5.20	190.81	3.90e7	6590.37	1.74	8.26e7	55.83	5.90e-16	0.97
5	8.66	312.79	2.40e7	3869.52	2.33	4.99e6	142.81	4.76e-14	0.95
7	12.12	698.36	4.93e7	15121.69	4.67	1.01e7	66.39	6.88e-19	0.97

suggesting that the creep model can describe the shear creep characteristics of the carbon mudstone. Thus, the applicability of the nonlinear creep constitutive model is verified. The nonlinear viscous element can describe the characteristics of the accelerated creep stage of the carbon mudstone, but it may not be the best. The main reason is that the carbon mudstone is a nonlinear visco-elastoplastic geotechnical material. Therefore, it has a complex deformation mechanism. However, the nonlinear viscous element has difficulties to describe the complex properties of the geotechnical materials such as the weakening effect of the generation, expansion, and convergence of the microcracks (Wang et al. 2017). In addition, the nonlinear viscous element cannot separate the elastic and viscoplastic deformations from the total deformations, so that the viscoplastic deformation is likely to contain the elastic deformation and not solely the viscoplastic deformation (Tsai et al. 2008). Because of these drawbacks, it can only generally describe the accelerated creep process of the rock mass. Thus, the creep deformation process of carbon mudstone cannot be predicted perfectly. In the future, we will try to take these factors into consideration to improve the prediction accuracy of the shear creep model.

According to the shear creep experimental results, the parameters of the modified creep model were acquired. In this study, the least-squares method was used to identify the shear creep parameters of carbon mudstone. Based on the experimental results, the model parameters of the carbon mudstone at the failure shear stress level under different normal stress were obtained, as listed in Table 3. Since carbon mudstone is a nonlinear elasto-viscoplastic body, that is, the creep compliance is not only a function of time, but also related to the stress level (Gao 2016), the coefficients of the creep model are different attributes to the nonlinear visco-elastoplastic deformation of carbon mudstone. Considering the complexity of rock mass in practical engineering and uncertain factors in the experiments, emphasizing the difference in creep model parameters under different shear stress levels may not necessarily improve the calculation accuracy (Gao 2016). Therefore, when performing rheological analysis, we still assume that the rheological parameters of the rock mass are constant under various shear loadings. Generally, the average value of model parameters of various shear stress levels can be used to reduce the uncertainty of model parameters at different shear stress levels (Gao 2016).

6 The stability of the slope considering the weak interlayer creep behaviors

6.1 The shear strength parameters considering the time effect

The failure of the rock mass is often related to its long-term strength. If the stress applied on the rock mass is less than the long-term strength, the rock will not undergo creep failure. For

Table 4 Ultimate strain under different normal stress of carbon mudstone

Normal stress (MPa)	3	5	7	Mean value
γ_l (10^{-3})		28.298	32.926	29.133	30.119

Table 5 Dynamic shear strength parameters of carbon mudstone

Time (a)	1	2	3	4	5	10
Equivalent cohesion c (kPa)	75.74	62.02	55.07	50.57	47.31	38.40
Equivalent friction angle φ (°)	20.74	17.23	15.39	14.19	13.31	10.87

shear creep, the long-term shear strength has a strong relationship with the normal stress. Correspondingly, when a rock undergoes creep failure, the rock also corresponds to an ultimate strain, and the ultimate strain is constant for the same kind of rock mass. It has nothing to do with the stress and the duration of failure time is irrelevant (Yang et al. 2014). In the shear rheological test, when the shear stress is applied step by step under any normal stress, the total strain at the failure point is also very close (Yang et al. 2011). The transition point from the steady creep stage to the accelerated creep stage is regarded as the critical point at which the rock mass enters the failure state, and the strain value at this critical point is regarded as the ultimate strain of the rock mass. At this time, the ultimate strain γ_l is used as the failure standard of rock creep and it is not affected by conditions such as normal stress. Based on the experimental results, the ultimate strain of carbon mudstone under different normal stress is listed in Table 4.

When geotechnical material strength weakens, it is usually manifested as a decrease in the shear strength parameter c and φ. Substituting the average value of the ultimate strain of the rock under different normal stress conditions into the modified creep model (Eq. (8)), the long-term shear stress of the carbon mudstone under different normal stress conditions can be obtained. Thereafter the dynamic shear strength parameters changing with time can be calculated by the Mohr–Coulomb strength criterion. The results are listed in Table 5.

6.2 The stability evolution law of the slope

Due to the continuous deformation of the south slope, the mine adopts backfill presser foot method to prevent further deformation of the slope. To study the deformation law of the south slope after the implementation of the backfill presser foot, the numerical simulation is used. Thus the numerical model was established as shown in Fig. 16. The numerical model is 6600 m in the X direction and 3700 m in the Y direction, and the height is 1810 m. The model was restrained in the normal direction and in the X and Y directions, the bottom was fixed and the slope surface was free. The tectonic stress was the stress induced by gravity. The Mohr–Coulomb constitutive model and the shear strength reduction method were used in the simulation. The model had nine different materials, including eight rock stratums and fault f5, as shown in Fig. 16. Meanwhile, the dynamic shear strength parameters of the weak layer were used as listed in Table 5. The parameters of other layers can be obtained from the previous studies and literature as listed in Table 6 (Zhang et al. 2019; CCTEG 2013, 2015). In order to study the stability of the slope, and further acquire the stress distribution in the slope, three transverse sections of I–I, II–II, and III–III were selected to study the internal stress change in the slope, and the position of the section is shown in Fig. 16.
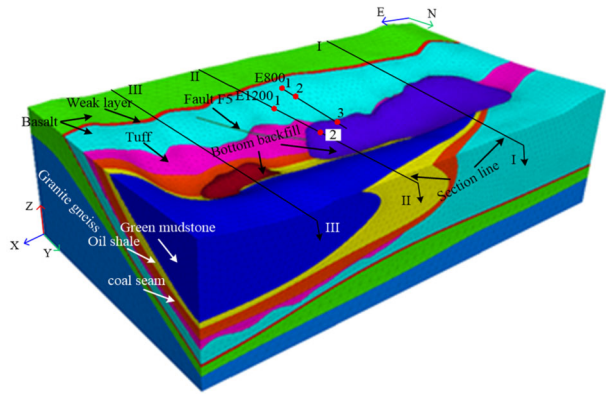
Fig. 16 Numerical simulation model

Table 6 Mechanic parameters of the rock mass of the south slope

Lithology	Young's modulus (GPa)	Poisson ratio	Cohesion (MPa)	Friction angle (°)	Density (kg m^{-3})
Basalt	7	0.14	0.14	42	2800
Granite Gneiss	8	0.2	0.2	45	2800
Weak layer (initial value)	0.1	0.4	0.076	20.74	2300
Coal seam	1.2	0.24	0.14	35	1300
Fault f5	0.1	0.4	0.012	7	1800
Oil shale	3.4	0.26	0.2	35	2300
Green mudstone	1.2	0.28	0.15	28	2300
Backfill	1.2	0.3	0.1	30	1800
Tuff	0.4	0.2	0.09	25	2300

From the calculation results of the slope after one year (Figs. 17(a)–(b)), it can be seen from the maximum stress contour that there is some tensile stress concentrated at the top of the slope. At this time, there is no obvious tensile stress concentration at the bottom of the open pit. The tensile stress concentration only occurs at the west side of the pit in the backfill intersection region of the slope. As time increases, the stress concentration range on the slope surface also increases (Figs. 17(c)–(d)). The range of stress concentration is gradually shifted to the upper part of the west region of the slope. At the same time, it can be seen that the shear stress concentration has also appeared at the bottom of the east region of the open pit. As time passes, the stress concentration range gradually increases. It can be seen that as time continues to increase, the range of tensile stress concentration does not increase significantly.

To further clarify the stress changing law inside the slope, three typical transverse sections of the slope are analyzed. Due to the similarity and gradual change law of the stress in the slope, only the simulation results after one and ten years are presented here, see Figs. 18 and 19. From the calculation results after one year, due to the existence of the weak layer, the maximum principal stress contour is redistributed near the weak layer, and there is a certain degree of tensile stress concentration at the top of the slope. It can be found that, due to the low strength of the weak layer, the maximum shear stress contour around the weak layer has also been redistributed, and there is an obvious shear stress concentration phenomenon
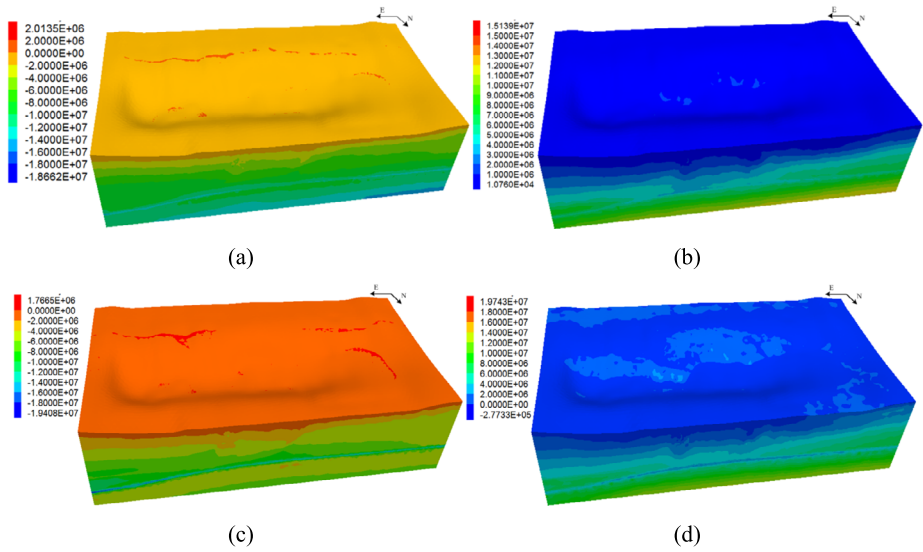
Fig. 17 The stress distribution of south slope: (a) maximum stress contour after one year; (b) maximum shear stress contour after one year; (c) maximum stress contour after ten years; (d) maximum shear stress contour after ten years
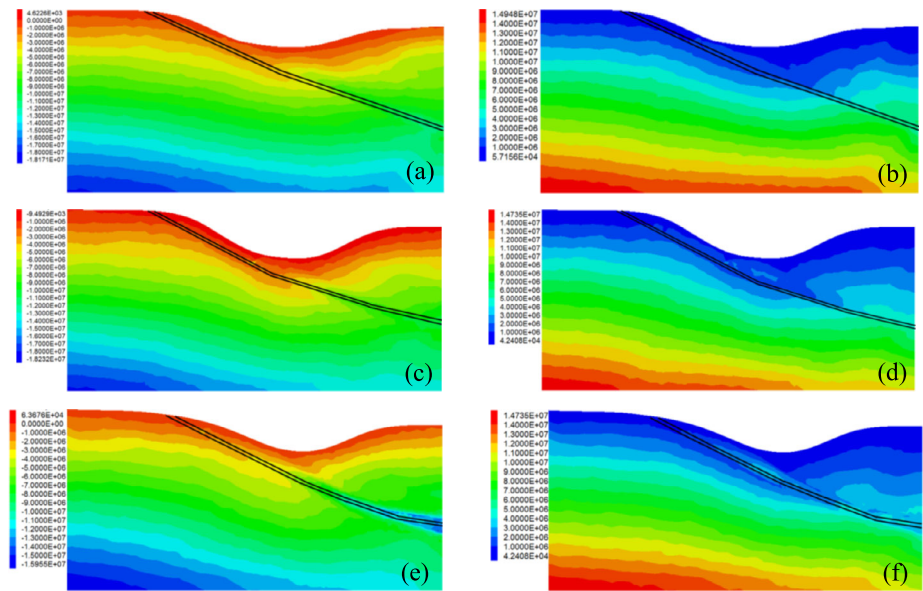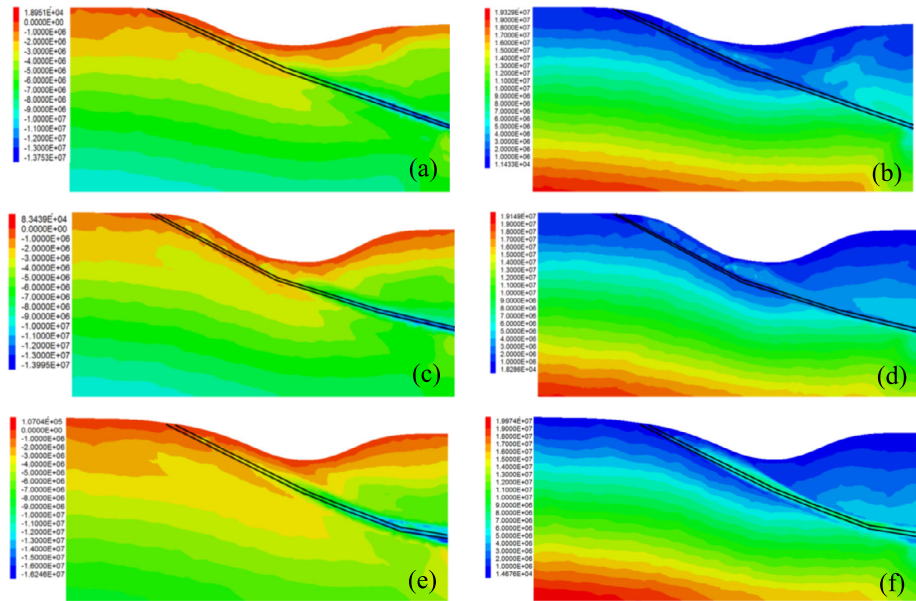

Fig. 18 The stress distribution of south slope after one year: (a) maximum stress contour of section I–I; (b) maximum shear stress contour of section I–I; (c) maximum stress contour of section II–II; (d) maximum shear stress contour of section II–II; (e) maximum stress contour of section III–III; and (f) maximum shear stress contour of section III–III

Fig. 19 The stress distribution of south slope after ten years: (a) maximum stress contour of section I–I; (b) maximum shear stress contour of section I–I; (c) maximum stress contour of section II–II; (d) maximum shear stress contour of section II–II; (e) maximum stress contour of section III–III; and (f) maximum shear stress contour of section III–III

at the position above the weak layer. In addition, shear stress is obvious at the bottom of the open pit in section II–II. After ten years, it can be seen from the maximum principal stress contour that the tensile stress concentrated near the weak layer has increased. It can be found from the maximum shear stress contour that the shear stress in the rock mass above the weak layer has concentrated in a larger area.

The factor of safety (FOS) of the slope is obtained using the strength reduction method. The FOS developing trend of the slope is shown in Fig. 20.

From Fig. 20, it can be seen that after the reinforcement of backfill presser foot project, the stability of the slope has improved significantly. However, with the increase of time, the FOS of the slope gradually decreases. After ten years, the FOS of the slope will reduce to 1.15, and the slope may once again enter the stage of accelerated creep deformation.

To further understand the stability of the slope after backfilling, the displacement monitoring was carried out on the surface of the slope. The on-site monitoring was started on December 31, 2012, and continued until June 14, 2018. Due to the large deformation which had occurred in the west region of the south slope, the monitoring point was mainly concentrated on two sections including E800 and E1200 in the west region. There were 5 monitoring points in total. In order to investigate the deformation features of the slope, the corresponding monitoring points were also selected on the surface of the numerical model. The distribution of the monitoring points is shown in Fig. 16, and the result is shown in Fig. 21.

It can be seen from the slope displacement curve that since 2013 the maximum displacement of the slope has reached 6 m. The presser foot project was ended in 2014. It can be found that the deformation continued to increase from 2013 to 2014, but with the implementation of the backfill presser foot project, the deformation rate of the slope has decreased significantly since 2015. In 2015, the maximum displacement of the slope was reduced to

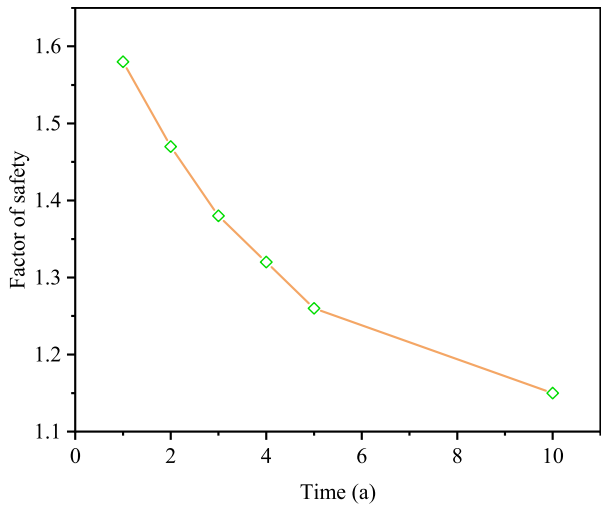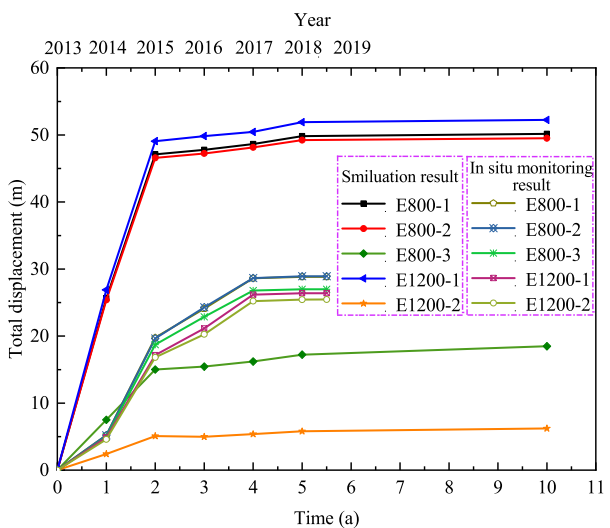**Fig. 20** FOS developing trend of the slope

Fig. 21 The total displacement curve obtained by simulation and on-site

4.8 m per year, which was significantly lower than the displacement of 16.4 m in 2014. The increase of displacement in 2016 was close to that of 2015. In 2017, the displacement of the slope decreased significantly, and the slope once again entered the steady deformation stage. With the implementation of the backfill presser foot project, the deformation of the slope was gradually controlled. The deformation state of the slope has gradually changed from an accelerating creep deformation to a decelerating creep deformation. Finally, the deformation of the slope appeared to be stable and entered the steady creep deformation stage. Combining the on-site monitoring displacement and numerical simulation results (Fig. 21), it can be seen from the numerical simulation results that the trend of the slope displacement is basically consistent with the in-situ monitoring results. This also further validates the reliability of the proposed creep model.
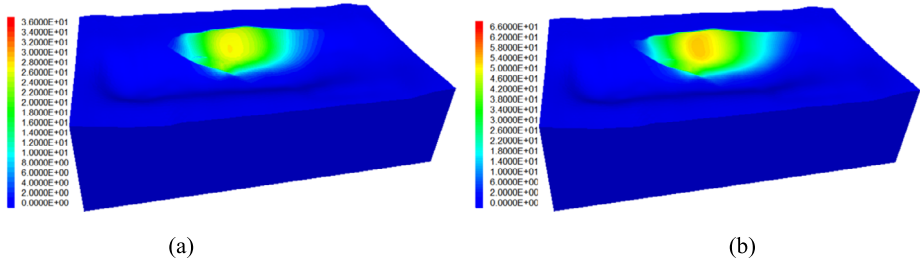
Fig. 22 The displacement contour of the south slope after strength reduction: (a) macroscopic displacement distribution after one year; (b) macroscopic displacement distribution after ten years

It can be seen from the simulation monitoring results that at the beginning of the second year, the deformation rate dropped significantly, and the slope entered the decelerating creep stage. After five years, the slope deformation rate has further decreased, and the slope has gradually entered the steady deformation stage. It also can be found that, at the two monitoring points E800-3 and E1200-2 located at the bottom of the open pit, the displacement is smaller than that of the upper monitoring points. The main reason is that they are affected by the backfill presser foot project. This shows that the backfill presser foot project first effectively restrained the deformation of the slope at the bottom. Figure 22 presents the distribution of the macroscopic displacement. It can be seen from the results that the large displacement is mainly concentrated in the west region of fault f5. It can be found that the macroscopic displacement pattern is similar after ten years. But the magnitude of the displacement is different from that after one year.

7 Conclusions

In this study, the creep behavior and the damage evolution of the carbon mudstone was studied to clarify the mechanism of the strength reduction effect on the stability of the slope. The creep deformation and cracking evolution of the specimens were analyzed. Moreover, the dynamic shear strength parameters were obtained and the stability of the large bedding slope was investigated. Based on the obtained results, the following conclusions can be drawn:

(1) There is an exponential relationship between the steady creep rate and the shear stress. Moreover, there is a strain threshold for the appearance of the accelerated creep stage.

(2) The shear strain will concentrate before the appearance of the macroscopic cracks. Carbon mudstone fails along a shear band rather than a shear surface, meanwhile, some tension fractures can be observed in the shear surface.

(3) Based on the creep behaviors of the carbon mudstone, a nonlinear elastic-viscoplastic shear creep model was established. Combining the creep model with the ultimate strain, the dynamic shear strength parameters of the carbon mudstone can be obtained.

(4) At the initial stage of the implementation of slope backfill presser foot, the deformation of the slope tends to the appearance of the accelerated deformation stage. With the increase of time, the slope deformation rate gradually decreases till the steady stage. The backfill presser foot project effectively prevents the slope before sliding. The results obtained in this study can help the decision-makers understand the deformation trend of the slope.

References

CCTEG Shenyang research Institute: Evaluation of Reinforcement Effect of Micro-Pile Structures in Fushun West Open-Pit Mine, pp. 1–11. CCTEG Shenyang research Institute, Fushun (2015) (in Chinese)

CCTEG Shenyang research Institute. Shenyang research Institute: Investigation on the Stability of South Slope of Fushun West Open-Pit Mine, pp. 1–94. CCTEG Shenyang research Institute, Fushun (2013) (in Chinese)

Chang, Z., Gao, H., Huang, F., et al.: Study on the creep behaviours and the improved Burgers model of a loess landslide considering matric suction. Nat. Hazards **103**, 1479–1497 (2020)

Chen, L., Li, S., Zhang, K., et al.: Secondary development and application of the NP-T creep model based on FLAC 3D. Arab. J. Geosci. **10**(23), 1–11 (2017)

Deng, H.F., Zhou, M.L., Li, J.L., et al.: Creep degradation mechanism by water-rock interaction in the red-layer soft rock. Arab. J. Geosci. **9**(12), 1–12 (2016)

Fu, T.F., Xu, T., Heap, M.J., et al.: Mesoscopic time-dependent behavior of rocks based on three-dimensional discrete element grain-based model. Comput. Geotech. **121**, 103472 (2020)

Gao, C.Y.: Study on Rheological Properties and Constitutive Model of Surrounding Rock in Zhuji Coal Mine Roadway. Doctor thesis, China University of Mining & Technology, Beijing (2016) (in Chinese)

Gao, C.Y., Gao, Q.C., Niu, J.G.: Nonlinear visco-elastic-plastic creep model in consideration of accelerated creep for sandrock in deep mine. J. Yangtze River Sci. Res. Inst. **33**(12), 99–104 (2016) (in Chinese)

He, Z.L., Zhu, Z.D., Ni, X.H., et al.: Shear creep tests and creep constitutive model of marble with structural plane. Eur. J. Environ. Civ. Eng. **23**(11), 1275–1293 (2019)

Hou, F., Lai, Y., Liu, E., et al.: A creep constitutive model for frozen soils with different contents of coarse grains. Cold Reg. Sci. Technol. **145**, 119–126 (2018)

Hou, R., Zhang, K., Tao, J., et al.: A nonlinear creep damage coupled model for rock considering the effect of initial damage. Rock Mech. Rock Eng. **52**(5), 1275–1285 (2019)

Huang, M., Zhan, J.W., Xu, C.S., et al.: New creep constitutive model for soft rocks and its application in the prediction of time-dependent deformation in tunnels. Int. J. Geomech. **20**(7), 04020096 (2020)

Huang, P., Zhang, J., Damascene, N.J., et al.: A fractional order viscoelastic-plastic creep model for coal sample considering initial damage accumulation. Alex. Eng. J. **60**(4), 3921–3930 (2021)

Lade, P.V., Liggio, C.D. Jr., Nam, J.: Strain rate, creep, and stress drop-creep experiments on crushed coral sand. J. Geotech. Geoenviron. Eng. **135**(7), 941–953 (2009)

Lai, X., Wang, S., Qin, H., et al.: Unsaturated creep tests and empirical models for sliding zone soils of Qianjiangping landslide in the Three Gorges. J. Rock Mech. Geotech. Eng. **2**(2), 149–154 (2010)

Li, Z., Cheng, P.: A study on the prediction of displacement in the accelerated deformation stage of the creep bedding rock landslides. Arab. J. Geosci. **14**(2), 1–11 (2021)

Li, W., Han, Y., Wang, T., et al.: DEM micromechanical modeling and laboratory experiment on creep behavior of salt rock. J. Nat. Gas Sci. Eng. **46**, 38–46 (2017)

Li, C., Tang, H., Han, D., et al.: Exploration of the creep properties of undisturbed shear zone soil of the Huangtupo landslide. Bull. Eng. Geol. Environ. **78**(2), 1237–1248 (2019)

Lin, H., Zhang, X., Cao, R., et al.: Improved nonlinear Burgers shear creep model based on the time-dependent shear strength for rock. Environ. Earth Sci. **79**(6), 1–9 (2020)

Liu, K., Zhao, J.: Progressive damage behaviours of triaxially confined rocks under multiple dynamic loads. Rock Mech. Rock Eng. **54**, 3327–3358 (2021)

Liu, W., Zhang, X., Li, H., et al.: Investigation on the deformation and strength characteristics of rock salt under different confining pressures. Geotech. Geolog. Eng. **38**, 5703–5717 (2020a)

Liu, Z., Zhou, C., Li, B., et al.: Effects of grain dissolution–diffusion sliding and hydro-mechanical interaction on the creep deformation of soft rocks. Acta Geotech. **15**(5), 1219–1229 (2020b)

Liu, X., Li, D., Han, C.: Nonlinear damage creep model based on fractional theory for rock materials. Mech. Time-Depend. Mater. **25**, 341–352 (2021)

Manconi, A., Kourkouli, P., Caduff, R., et al.: Monitoring surface deformation over a failing rock slope with the ESA sentinels: insights from Moosfluh instability, Swiss Alps. Remote Sens. **10**(5), 672 (2018)

Mikroutsikos, A., Theocharis, A.I., Koukouzas, N.C., et al.: Slope stability of deep surface coal mines in the presence of a weak zone. Geomech. Geophys. Geo-Energy Geo-Resour. **7**(3), 1–17 (2021)

Rahardjo, H., Kim, Y., Gofar, N., et al.: Field instrumentations and monitoring of GeoBarrier System for steep slope protection. Transp. Geotech. **16**, 29–42 (2018)

Sun, M., Tang, H., Wang, M., et al.: Creep behavior of slip zone soil of the Majiagou landslide in the Three Gorges area. Environ. Earth Sci. **75**(16), 1–12 (2016)

Tsai, L.S., Hsieh, Y.M., Weng, M.C., et al.: Time-dependent deformation behaviours of weak sandstones. Int. J. Rock Mech. Min. Sci. **45**, 144–154 (2008)

Wang, Y., Li, J.L., Liu, F.: Experimental research on shear creep and its long-term strength of weak intercalation in dam foundation. Chin. J. Rock Mech. Eng. **32**(S2), 3378–3384 (2013) (in Chinese)

Wang, Q.Y., Zhu, W.C., Xu, T., et al.: Numerical simulation of rock creep behavior with a damage-based constitutive law. Int. J. Geomech. **17**(1), 04016044 (2017)

Wang, J., Sun, Q., Liang, B., et al.: Mudstone creep experiment and nonlinear damage model study under cyclic disturbance load. Sci. Rep. **10**(1), 1–11 (2020)

Wei, Y., Chen, Q., Huang, H., et al.: Study on creep models and parameter inversion of columnar jointed basalt rock masses. Eng. Geol. **290**, 106206 (2021)

Wu, C., Chen, Q., Basack, S., et al.: Biaxial creep test study on the influence of structural anisotropy on rheological behavior of hard rock. J. Mater. Civ. Eng. **28**(10), 04016104 (2016)

Wu, L., Li, B., Sun, P.: Study on shear creep behavior of mudstone and its correction model of Gangu fissure in Gansu. J. Geomech. **23**(6), 923–934 (2017)

Wu, L.Z., Li, S.H., Sun, P., et al.: Shear creep tests on fissured mudstone and an improved time-dependent model. Pure Appl. Geophys. **176**(11), 4797–4808 (2019)

Wu, F., Zhang, H., Zou, Q., et al.: Viscoelastic-plastic damage creep model for salt rock based on fractional derivative theory. Mech. Mater. **150**, 103600 (2020)

Xu, N.W., Tang, C.A., Li, L.C., et al.: Microseismic monitoring and stability analysis of the left bank slope in Jinping first stage hydropower station in southwestern China. Int. J. Rock Mech. Min. Sci. **48**(6), 950–963 (2011)

Xu, T., Qiang, X., Tang, C.A., et al.: The evolution of rock failure with discontinuities due to shear creep. Acta Geotech. **8**(6), 567–581 (2013)

Xu, T., Xu, Q., Deng, M., et al.: A numerical analysis of rock creep-induced slide: a case study from Jiweishan Mountain, China. Environ. Earth Sci. **72**(6), 2111–2128 (2014)

Yang, T.H., Rui, Y.Q., Shen, L., et al.: Dynamic Stability and Control Technology of Open Pit Slope Under Seepage. The Science Publishing Company, Beijing (2011)

Yang, T., Xu, T., Liu, H., et al.: Rheological characteristics of weak rock mass and effects on the long-term stability of slopes. Rock Mech. Rock Eng. **47**(6), 2253–2263 (2014)

Yang, S.Q., Chen, M., Huang, Y.H., et al.: An experimental study on fracture evolution mechanism of a non-persistent jointed rock mass with various anchorage effects by DSCM, AE and X-ray CT observations. Int. J. Rock Mech. Min. Sci. **134**, 104469 (2020)

Yu, X.Y., Xu, T., Heap, M., et al.: Numerical approach to creep of rock based on the numerical manifold method. Int. J. Geomech. **18**(11), 04018153 (2018)

Yuan, Y., Xu, T., Heap, M.J., et al.: A three-dimensional mesoscale model for progressive time-dependent deformation and fracturing of brittle rock with application to slope stability. Comput. Geotech. **135**, 104160 (2021)

Zhang, F., Yang, T.H., Li, L.C., Wang, Z., Xiao, P.: Cooperative monitoring and numerical investigation on the stability of the south slope of the Fushun West Open-pit mine. Bull. Eng. Geol. Environ. **78**(4), 2409–2429 (2019)

Zhao, Y., Wang, Y., Wang, W., et al.: Modeling of non-linear rheological behavior of hard rock using triaxial rheological experiment. Int. J. Rock Mech. Min. Sci. **93**, 66–75 (2017)

Zhao, H., Tian, Y., Guo, Q., et al.: The slope creep law for a soft rock in an open-pit mine in the Gobi region of Xinjiang, China. Int. J. Coal Sci. Technol. **7**(2), 371–379 (2020a)

Zhao, T., Zhang, W., Gu, S., et al.: Study on fracture mechanics of granite based on digital speckle correlation method. Int. J. Solids Struct. **193**, 192–199 (2020b)

Zhou, Z., Chen, L., Cai, X., et al.: Experimental investigation of the progressive failure of multiple pillar–roof system. Rock Mech. Rock Eng. **51**(5), 1629–1636 (2018)

Zhou, G., Xu, T., Heap, M.J., et al.: A three-dimensional numerical meso-approach to modeling time-independent deformation and fracturing of brittle rocks. Comput. Geotech. **117**, 103274 (2020)